Available online at www.sciencedirect.com
ScienceDirect
Journal of Computational Physics 226 (2007) 1256–1270
JOURNAL OF COMPUTATIONAL PHYSICS
www.elsevier.com/locate/jcp

An efficient semi-implicit compressible solver for large-eddy simulations

V. Moureau [a,*], C. Bérat [b], H. Pitsch [a]

[a] Center for Turbulence Research, Stanford University, Stanford, CA 94305, USA
[b] Turboméca – Safran Group, 64522 Bordes, France

Received 15 March 2006; received in revised form 10 May 2007; accepted 22 May 2007
Available online 16 June 2007

Abstract

In this paper, a pressure-based semi-implicit algorithm for compressible flows is described. This type of solver is of great interest in combustion devices where the flow speed is small but where the unsteady heat release can be coupled to the acoustic modes and lead to instabilities. The fractional-step method used in this algorithm is based on a characteristic splitting, which clearly separates the acoustics from the advection. This splitting allows to use adapted numerics for these different time-scales. The algorithm is second-order in space and time for linear acoustics and for low-Mach advection without iterating the time-step. Moreover, when kinetic-energy conserving schemes are used for the predictor step, the algorithm discretely conserves the kinetic energy in the low-Mach limit. All these properties are illustrated on simple test cases and the algorithm is finally validated by performing the LES of the cold flow of an industrial burner.

Keywords: LES; Semi-implicit; Compressible; Fractional-step method; Unstructured grids

1. Motivation and objectives

In most combustion devices, the Mach number is small, and the most efficient computational approach is the solving of the low-Mach number formulation of the Navier–Stokes equations. In this approach, the acoustic waves propagate at an infinite speed. Nevertheless, when the acoustic speed plays an important role, as in the formation of instabilities in cavities, the compressible Navier–Stokes equations must be solved. If these equations are solved explicitly, the acoustic CFL condition imposes a drastic limit on the time-step for flows of low convective CFL number. Then, a semi-implicit approach, in which acoustic waves are solved implicitly, potentially offers significant efficiency gains using larger time-steps.

Implicit compressible solvers able to deal with low-Mach number flows fall into two basic categories. The first category consists of the density-based solvers, which are originally designed for high-Mach number flows. When the Mach number goes to zero, the algebraic system of these solvers becomes ill-conditioned [1,2].

* Corresponding author.
E-mail address: vincent.moureau@centraliens.net (V. Moureau).

0021-9991/$ - see front matter
doi:10.1016/j.jcp.2007.05.035

This issue is classically overcome using preconditioning techniques [3] or by performing a Taylor-series expansion in Mach number [4]. The second category is that of the pressure-based solvers. These solvers were originally developed for incompressible flows. For this type of flows, the pressure gradient in the momentum equation acts as a source term needed to maintain the incompressibility constraint. This dynamic pressure comes from the solution of a Poisson equation, which is elliptic. In pressure-based compressible solvers, the Poisson equation becomes a Helmholtz equation, which propagates the pressure waves with a finite speed and which is thus hyperbolic. Solving a pressure equation ensures that in contrast to non-preconditioned density-based systems, the pressure variations remain finite in the low-Mach limit. Many pressure-based implicit compressible solvers have been designed since the pioneering work of [5]. Unfortunately, these methods are either first-order in time [6], non-mass conservative [7], or they necessitate a very costly inner loop to couple the energy (or enthalpy) equation to the other equations [8,9]. This inner loop simply consists in iterating the full time-step to obtain the coupling.

A suitable method for the computation of acoustic instabilities in a combustion device needs to be mass conservative and efficient, which precludes the use of an inner loop to converge the energy equation, and it has to be low-dissipative. In this paper, a method that fulfills these requirements is proposed. It is a fractional-step method [10] based on a characteristic splitting. This method consists of an advection or predictor step, and a pressure-correction step. In the pressure-correction step, a Helmholtz equation is solved implicitly to remove the acoustic CFL condition. The characteristic splitting allows the decoupling of the acoustic waves from the advection, and as a result a second-order spatial and temporal convergence for linear acoustics is obtained without inner loop. When this method is used in combination with a kinetic-energy conserving scheme for the advection step [11], the method is kinetic-energy conserving in the incompressible limit.

The proposed method is verified by performing simple test cases. The first test is a linear acoustic wave propagation, the second test is a low-Mach vortex advection, and the third test consists of the computation of an under-resolved homogeneous isotropic turbulence (HIT) case at an infinite Reynolds number. These tests are performed to demonstrate all the properties mentioned above. Finally, the new compressible solver is applied in an LES computation of the cold flow of an industrial lean-premixed burner. This computation has also been performed with an incompressible solver with the same mean convective CFL and the same spatial and temporal schemes. It is demonstrated that the computational time required for the fully compressible simulation is only slightly higher than when using a low-Mach number solver. All these test cases show that the present method is able to compute efficiently low-Mach number flows while transporting the acoustic waves at the correct speed. These two aspects are essential to build any solver for the analysis of combustion instabilities.

2. Fractional-step methods for low-Mach number flows

In this section, the original fractional-step method of Kim and Moin [10] for constant-density flows is presented as well as its extension to variable-density flows [12]. In these two methods, the Mach number is considered small enough so that the pressure variations are decoupled from the density variations at constant entropy. It means that the speed of the acoustic waves tends to be infinite and the continuity equation acts as a constraint on the velocity divergence. In the case of a constant-density flow, the velocity divergence is simply zero. In the more general case of a variable-density flow with a low-Mach number, the continuity relates the velocity divergence to the density variations that are obtained from an energy equation and from the equation-of-state where the thermodynamic pressure, also called the background pressure, is taken constant.

2.1. The fractional-step method of Kim and Moin [10] for incompressible flows

Considering an incompressible constant-density flow, the continuity equation reduces to:

$$\nabla \cdot (\bar{\mathbf{u}}) = 0, \tag{1}$$

and the velocity equation reads:

$$\frac{\partial \bar{\mathbf{u}}}{\partial t} + \nabla \cdot (\bar{\mathbf{u}}\bar{\mathbf{u}}) = -\frac{1}{\rho}\nabla \overline{P} + \frac{1}{\rho}\nabla \cdot \mathbf{t}, \tag{2}$$

where $\bar{}$ denotes the LES filtering, ρ is the constant density, $\mathbf{u}$ is the velocity, P is the pressure and $\mathbf{t}$ is the total stress tensor. The pressure in (2) is not the thermodynamic pressure of the equation-of-state but rather a Lagrange multiplier also called dynamic pressure.

The fractional-step method of Kim and Moin [10] consists of two steps. The first step is the predictor step:

$$\frac{\bar{\mathbf{u}}^{\star} - \bar{\mathbf{u}}^{n}}{\Delta t} + \nabla \cdot (\bar{\mathbf{u}}^{n+1/2}\bar{\mathbf{u}}^{n+1/2}) = \frac{1}{\rho}\nabla \cdot \mathbf{t}. \tag{3}$$

In the second step, the velocity is corrected with the dynamic pressure gradient:

$$\frac{\bar{\mathbf{u}}^{n+1} - \bar{\mathbf{u}}^{\star}}{\Delta t} = -\frac{1}{\rho}\nabla \overline{P}^{n+1/2}. \tag{4}$$

The dynamic pressure $\overline{P}^{n+1/2}$ is found by solving the Poisson equation that is obtained by taking the divergence of (4) and by using $\nabla \cdot (\bar{\mathbf{u}}^{n+1}) = 0$:

$$\nabla \cdot \nabla \overline{P}^{n+1/2} = \frac{1}{\Delta t}\nabla \cdot (\bar{\mathbf{u}}^{\star}). \tag{5}$$

2.2. The fractional-step method of Pierce and Moin [12] for variable-density and low-Mach number flows

In reacting flows, due to thermal expansion, the density is not constant and the incompressible method of Kim and Moin [10] cannot be used. Then, the continuity and momentum equations are:

$$\frac{\partial \bar{\rho}}{\partial t} + \nabla \cdot (\bar{\rho}\tilde{\mathbf{u}}) = 0 \tag{6}$$

$$\frac{\partial \bar{\rho}\tilde{\mathbf{u}}}{\partial t} + \nabla \cdot (\bar{\rho}\tilde{\mathbf{u}}\tilde{\mathbf{u}}) = -\nabla \overline{P} + \nabla \cdot \mathbf{t}, \tag{7}$$

where $\tilde{}$ denotes the density-weighted LES filtering. In the low-Mach limit, the dynamic pressure variations are decoupled from the density variations and the density is simply an input of Eqs. (6) and (7). The density can be determined by transporting an energy equation and by using the equation-of-state with a constant background pressure. Alternatively, the density can be tabulated as a function of a progress-variable, a mixture fraction and its variance [13]. Once the density is given by the combustion model, the momentum equation (7) can be solved using a fractional-step method. A time-staggered discretization of (6) is given as:

$$\frac{\bar{\rho}^{n+3/2} - \bar{\rho}^{n+1/2}}{\Delta t} + \nabla \cdot (\bar{\rho}\tilde{\mathbf{u}}^{n+1}) = 0, \tag{8}$$

and the predictor step of the fractional-step method is to advance the momentum equation:

$$\frac{\bar{\rho}\tilde{\mathbf{u}}^{\star} - \bar{\rho}\tilde{\mathbf{u}}^{n}}{\Delta t} + \nabla \cdot (\bar{\rho}\tilde{\mathbf{u}}^{n+1/2}\tilde{\mathbf{u}}^{n+1/2}) = \nabla \cdot \mathbf{t}. \tag{9}$$

In the second step, the momentum is corrected with the dynamic pressure gradient:

$$\frac{\bar{\rho}\tilde{\mathbf{u}}^{n+1} - \bar{\rho}\tilde{\mathbf{u}}^{\star}}{\Delta t} = -\nabla \overline{P}^{n+1/2}. \tag{10}$$

The dynamic pressure $\overline{P}^{n+1/2}$ is found by solving the variable-density Poisson equation:

$$\nabla \cdot \nabla \overline{P}^{n+1/2} = \frac{\bar{\rho}^{n+3/2} - \bar{\rho}^{n+1/2}}{\Delta t^2} + \frac{1}{\Delta t}\nabla \cdot (\bar{\rho}\tilde{\mathbf{u}}^{\star}). \tag{11}$$

Equation (11) is elliptic, meaning that a variation of the RHS generates a pressure wave that propagates at an infinite speed. Thermo-acoustic instabilities for instance, which consist of a two-way coupling of the heat release of the flame with the acoustics of the combustion chamber, cannot be predicted by using this method.

To predict these instabilities in usual combustion devices, a fully compressible algorithm is needed and it has to be effective even if the acoustic time-scale is one order of magnitude smaller than the convective time-scale.

3. A characteristic-based fractional-step method

In this section, the characteristic splitting of the Navier–Stokes equations is described first. Then, the full algorithm of the new semi-implicit compressible solver is presented and analyzed for linear acoustics and in the low-Mach limit.

3.1. Compressible large-eddy simulation equations

The compressible Navier–Stokes equations for the large-eddy simulation of a non-reactive flow are:

$$\frac{\partial \bar{\rho}}{\partial t} + \nabla \cdot (\bar{\rho}\tilde{\mathbf{u}}) = 0 \tag{12}$$

$$\frac{\partial \bar{\rho}\tilde{\mathbf{u}}}{\partial t} + \nabla \cdot (\bar{\rho}\tilde{\mathbf{u}}\tilde{\mathbf{u}}) = -\nabla \overline{P} + \nabla \cdot \mathbf{t} \tag{13}$$

$$\frac{\partial \bar{\rho}\tilde{h}}{\partial t} + \nabla \cdot (\bar{\rho}\tilde{h}\tilde{\mathbf{u}}) = \frac{\partial \overline{P}}{\partial t} + \tilde{\mathbf{u}} \cdot \nabla \overline{P} + \nabla \cdot ((\lambda + \lambda_t)\nabla \widetilde{T}) + \mathbf{t} \cdot \nabla \tilde{\mathbf{u}}. \tag{14}$$

$\tilde{h}$ is the sensible enthalpy defined by:

$$\tilde{h} = \int_{T_0}^{\widetilde{T}} C_p \, \mathrm{d}T. \tag{15}$$

The equation-of-state for a perfect-gas mixture is:

$$\overline{P} = \bar{\rho} r \widetilde{T}. \tag{16}$$

The speed of sound speed c at constant entropy is defined by:

$$c^2 = \left.\frac{\partial \overline{P}}{\partial \bar{\rho}}\right|_{\tilde{s}=\tilde{s}_0} = \gamma r \widetilde{T}. \tag{17}$$

To be able to perform the so-called characteristic splitting, the pressure has to be removed from the enthalpy equation (14). Taking the derivative of the equation-of-state (16) relates the enthalpy variations to the pressure and density variations:

$$\bar{\rho}\partial\tilde{h} = \bar{\rho} C_p \partial \widetilde{T} = \frac{\gamma}{\gamma - 1}\left(\partial \overline{P} - \frac{c^2}{\gamma}\partial\bar{\rho}\right), \tag{18}$$

and the enthalpy equation (14) is rewritten as follows:

$$\frac{\partial \bar{\rho}\tilde{h}}{\partial t} + \nabla \cdot (\bar{\rho}\tilde{h}\tilde{\mathbf{u}}) = -c^2\bar{\rho}\nabla \cdot \tilde{\mathbf{u}} + \gamma \nabla \cdot ((\lambda + \lambda_t)\nabla \widetilde{T}) + \gamma \mathbf{t} \cdot \nabla \tilde{\mathbf{u}}. \tag{19}$$

A similar equation for the pressure can be obtained from the enthalpy equation (19) and the derivative of the equation-of-state (18):

$$\frac{\partial \overline{P}}{\partial t} + \tilde{\mathbf{u}} \cdot \nabla \overline{P} = -c^2\bar{\rho}\nabla \cdot \tilde{\mathbf{u}} + (\gamma - 1)\nabla \cdot ((\lambda + \lambda_t)\nabla \widetilde{T}) + (\gamma - 1)\mathbf{t} \cdot \nabla \tilde{\mathbf{u}}. \tag{20}$$

3.2. Fractional-step method

The main idea of the method is to separate the convective and acoustic time-scales, which can be significantly different in low-Mach flows, to treat each of them with efficient algorithms. This can be achieved by splitting the eigenvalues of the 1D compressible Navier–Stokes equations:

$$\begin{pmatrix} u+c \\ u-c \\ u \end{pmatrix} = \begin{pmatrix} u \\ u \\ u \end{pmatrix} + \begin{pmatrix} c \\ -c \\ 0 \end{pmatrix}. \tag{21}$$

The two first eigenvalues on the LHS are the speeds of the two acoustic waves. The third eigenvalue corresponds to the advection. On the RHS, a pure advection step and a pure acoustic step are obtained. The proposed method extends this decomposition to the 3D Navier–Stokes equations as described below.

3.2.1. First step: advection

In this first step, all variables are advected. For $\phi \in \{\rho, \rho\mathbf{u}, \rho h\}$,

$$\frac{\bar{\phi}^\star - \bar{\phi}^n}{\Delta t} + \nabla\cdot(\bar{\phi}\tilde{\mathbf{u}}) - \bar{\phi}\nabla\cdot\tilde{\mathbf{u}} = D_\phi, \tag{22}$$

where the diffusion and dissipation terms are $D_\rho = 0$, $D_{\rho\mathbf{u}} = \nabla\cdot\mathbf{t}$ and $D_{\rho h} = \gamma\nabla\cdot((\lambda+\lambda_t)\nabla\widetilde{T}) + \gamma\mathbf{t}\cdot\vec{\nabla}\tilde{\mathbf{u}}$. At the end of this step, the pressure $\overline{P}^\star$ is estimated from $\bar{\rho}^\star$ and $\tilde{h}^\star$ using the equation-of-state (16).

3.2.2. Second step: pressure correction

The second step is obtained by removing (22) from the Navier–Stokes equations (12), (13) and (19):

$$\frac{\bar{\rho}^{n+1} - \bar{\rho}^\star}{\Delta t} + \bar{\rho}\nabla\cdot\tilde{\mathbf{u}} = 0 \tag{23}$$

$$\frac{\bar{\rho}\tilde{\mathbf{u}}^{n+1} - \bar{\rho}\tilde{\mathbf{u}}^\star}{\Delta t} + \bar{\rho}\tilde{\mathbf{u}}\nabla\cdot\tilde{\mathbf{u}} = -\nabla\left(\frac{\overline{P}^n + \overline{P}^{n+1}}{2}\right) \tag{24}$$

$$\frac{\bar{\rho}\tilde{h}^{n+1} - \bar{\rho}\tilde{h}^\star}{\Delta t} + \bar{\rho}\tilde{h}\nabla\cdot\tilde{\mathbf{u}} = -c^2\bar{\rho}\nabla\cdot\tilde{\mathbf{u}}. \tag{25}$$

The same type of equation is also obtained for the pressure from (20):

$$\frac{\overline{P}^{n+1} - \overline{P}^\star}{\Delta t} = -c^2\bar{\rho}\nabla\cdot\tilde{\mathbf{u}}. \tag{26}$$

(26) directly relates the pressure variations in the second step to the velocity divergence. This relation can be used to express (23)–(25) as functions of the pressure variations $\delta\overline{P} = \overline{P}^{n+1} - \overline{P}^\star$:

$$\frac{\bar{\rho}^{n+1} - \bar{\rho}^\star}{\Delta t} - \frac{1}{c^2}\frac{\delta\overline{P}}{\Delta t} = 0 \tag{27}$$

$$\frac{\bar{\rho}\tilde{\mathbf{u}}^{n+1} - \bar{\rho}\tilde{\mathbf{u}}^\star}{\Delta t} - \frac{\tilde{\mathbf{u}}}{c^2}\frac{\delta\overline{P}}{\Delta t} = -\nabla\left(\frac{\overline{P}^n + \overline{P}^{n+1}}{2}\right) \tag{28}$$

$$\frac{\bar{\rho}\tilde{h}^{n+1} - \bar{\rho}\tilde{h}^\star}{\Delta t} - \frac{\tilde{h}+c^2}{c^2}\frac{\delta\overline{P}}{\Delta t} = 0. \tag{29}$$

Taking the divergence of (28) and using the continuity equation to remove the unknown velocity $\bar{\rho}\tilde{\mathbf{u}}^{n+1}$ leads to the Helmholtz equation:

$$\nabla\cdot\nabla(\delta\overline{P}) - \nabla\cdot\left(\frac{2\tilde{\mathbf{u}}}{c^2\Delta t}\delta\overline{P}\right) - \frac{4}{c^2\Delta t^2}\delta\overline{P} = -\nabla\cdot\nabla(\overline{P}^\star + \overline{P}^n) + \frac{4}{\Delta t}\left(\frac{\bar{\rho}^\star - \bar{\rho}^n}{\Delta t} + \nabla\cdot\left(\frac{\bar{\rho}\tilde{\mathbf{u}}^\star + \bar{\rho}\tilde{\mathbf{u}}^n}{2}\right)\right). \tag{30}$$

The continuity equation used to remove the unknown velocity in the previous equation is a second-order time discretization of the continuity equation (12):

$$\frac{\bar{\rho}^{n+1} - \bar{\rho}^n}{\Delta t} + \nabla\cdot\left(\frac{\bar{\rho}\tilde{\mathbf{u}}^{n+1} + \bar{\rho}\tilde{\mathbf{u}}^n}{2}\right) = 0. \tag{31}$$

The use of the continuity equation to derive the Helmholtz equation ensures that the method is mass conservative.

When comparing this method to the variable-density algorithm of Pierce and Moin [12], the main difference appears in the pressure equation of the correction step. In the case of the variable-density low-Mach algorithm, it is a Poisson equation, and in this method this is a Helmholtz equation. It implies that the pressure fluctuations generated to balance local density variations do not propagate similarly in the two algorithms. The pressure fluctuations are propagated isotropically in all directions in the two algorithms but in the low-Mach algorithm their speed is infinite, and in the present method their speed is c. This means that the present method has the benefit of being able to predict the acoustic modes of a cavity or the coupling of a flame with acoustic waves that have similar time scales. This is not the case of the method of Pierce and Moin.

3.3. Full algorithm

The full algorithm described in this section is collocated. All the spatial operators are the numerics described in [14].

3.3.1. Step 1: predictor step

In this step, all the quantities are advected at the flow speed. (22) is solved implicitly by using a Gauss–Seidel method with relaxation for all the conservative variables. The divergence operator is the kinetic-energy conserving operator described in [11]. At the end of the step, the intermediate pressure $\overline{P}^{\star}$ is computed using the equation-of-state (16).

3.3.2. Step 2: pressure correction

The Helmholtz equation (30) is solved implicitly by using a Stabilized Bi-Conjugate-Gradient (BiCGStab) linear solver. Then, the pressure variations $\delta\overline{P}$ are used in (27)–(29) to obtain the values of the conservative variables at the end of the time-step. To avoid the pressure–velocity decoupling in the Helmholtz equation in the low-Mach limit, the technique of [14] is used. It consists of staggering the momentum-correction equation (28) to obtain a compact Laplacian operator in the Helmholtz equation.

The quantities without time index in (28) and (29) can be set equal to the value at the beginning of the time-step if no inner loop is used. This approximation does not affect the second-order temporal accuracy for the linear acoustics and for the low-Mach advection. For other cases, the second-order temporal accuracy is obtained by taking these values at the middle of the time-step and by performing at least two inner-loop iterations.

3.4. Boundary conditions

In the solver, walls are treated implicitly by setting the pressure gradient equal to zero in the Helmholtz equation and by imposing a no-slip velocity in the advection step. The resulting boundary conditions are acoustically reflecting no-slip walls. The inlets and outlets are treated explicitly with classical Navier–Stokes Characteristic Boundary Conditions (NSCBC) [15]. This explicit treatment is not time-step limiting for most computations because the smallest control volumes, which limit the acoustic time step, are usually not in the vicinity of the inlets and outlets.

3.5. Analysis

3.5.1. Linear acoustics

A linear acoustics analysis of the proposed method is performed. This analysis consists of adding a small perturbation $\bar{\phi}_1$ to a uniform flow $\bar{\phi}_0$:

$$\bar{\phi} = \bar{\phi}_0 + \bar{\phi}_1, \quad \text{with } \bar{\phi}_1 \ll \bar{\phi}_0. \tag{32}$$

The flow speed is assumed small, i.e. $\tilde{\mathbf{u}}_0 = 0$, and the viscous effects are neglected. The sound speed is also assumed constant. Introducing this decomposition in the advection step of the method (22) and keeping the first-order terms simply gives $\bar{\phi}_1^{\star} = \bar{\phi}_1^{n}$ for all the variables $\phi \in \{\rho, \rho\mathbf{u}, \rho h, P\}$. As expected, the first step has no effect on linear acoustics if the flow speed is zero. The same analysis is then performed for the pressure-correction step by using the fact that $\bar{\phi}_1^{\star} = \bar{\phi}_1^{n}$. The momentum equation (28) becomes:

$$\bar{\rho}_0 \frac{\tilde{\mathbf{u}}_1^{n+1} - \tilde{\mathbf{u}}_1^n}{\Delta t} + \nabla\left(\frac{\overline{P}_1^n + \overline{P}_1^{n+1}}{2}\right) = 0. \tag{33}$$

The density correction (27) combined with the continuity (31) leads to another relation between the velocity and the pressure:

$$\frac{1}{c^2}\frac{\overline{P}_1^{n+1} - \overline{P}_1^n}{\Delta t} + \bar{\rho}_0 \nabla \cdot \left(\frac{\tilde{\mathbf{u}}_1^{n+1} + \tilde{\mathbf{u}}_1^n}{2}\right) = 0. \tag{34}$$

Equations (33) and (34) are the classical linear acoustics relations discretized with a second-order temporal scheme. In the proposed method, a second-order central scheme is used for the spatial discretization so that the method is second-order in space and time for linear acoustics without inner loop.

3.5.2. Low-Mach limit

Investigating the behaviour of the algorithm in the low-Mach limit is very important, as in most practical combustion devices the Mach number $Ma = \tilde{\mathbf{u}}/c$ is small and as the compressible solvers may be ill-conditioned in this limit [2]. The Mach-dependence of each term in the Helmholtz equation can be analyzed. Multiplying (30) by the square of the cell-width Δx leads to:

$$\mathcal{O}(\delta\overline{P}) - \mathcal{O}(Ma^2 \mathrm{CFL}_{\mathrm{conv}}^{-1}\delta\overline{P}) - \mathcal{O}(Ma^2 \mathrm{CFL}_{\mathrm{conv}}^{-2}\delta\overline{P}) = -\mathcal{O}(\overline{P}^\star + \overline{P}^n) + \mathcal{O}\left(\frac{4\Delta x^2}{\Delta t}\left(\frac{\bar{\rho}^\star - \bar{\rho}^n}{\Delta t} + \nabla \cdot \left(\frac{\bar{\rho}\tilde{\mathbf{u}}^\star + \bar{\rho}\tilde{\mathbf{u}}^n}{2}\right)\right)\right), \tag{35}$$

where $\mathrm{CFL}_{\mathrm{conv}} = \tilde{\mathbf{u}}\Delta t/\Delta x$ is the convective Courant number. In the zero-Mach limit, the second and third terms of the LHS vanish, and the Helmholtz equation becomes the variable-density Poisson equation (11). Therefore, for small Mach numbers, the proposed method tends towards a variable-density low-Mach method, which is collocated in time, unlike the algorithm of Pierce and Moin [12], which is time-staggered. This implies that in the low-Mach limit, the method is well-posed and pressure fluctuations remain finite.

Moreover, if the density of the flow is constant, the third term on the LHS of (22), which is proportional to the velocity divergence, vanishes. Since a kinetic-energy conserving scheme [11] is used for the convective term, the advection step discretely conserves the kinetic-energy in the low-Mach limit.

3.5.3. Some remarks about the temporal accuracy of the method

The method is formally second-order in space and time for linear acoustics and for low-Mach advection. It means that the temporal error in the Helmholtz equation increases significantly when the acoustic CFL is higher than one. Nevertheless, as presented in the previous Section, the temporal error in the Helmholtz equation scales as Ma^2. It implies that even if the acoustic CFL is big, the temporal error will be small if the local Mach number is small. This is the case for the cells used to refine the mesh close to the walls of the device. In these regions, the Mach number is very small and the acoustic CFL is big because the cells are very small. From the experience of the authors, the temporal error has a negligible effect on the results if the regions where the acoustic CFL is big are very localized.

4. Results

In this section, the proposed method is verified by computing simple test cases. Then the method is applied in the computation of the cold flow of an industrial lean-premixed burner.

4.1. Convergence-order evaluation

4.1.1. Linear acoustics

A 1D Gaussian acoustic wave of small amplitude is propagated on a periodic mesh. The L2 error is computed after one acoustic time propagation. Figs. 1 and 2 present the spatial and the temporal convergence of the error. The spatial error is second-order, and the temporal error is slightly less than second-order. As expected, performing two inner-loops has no effect on the error for linear acoustics.

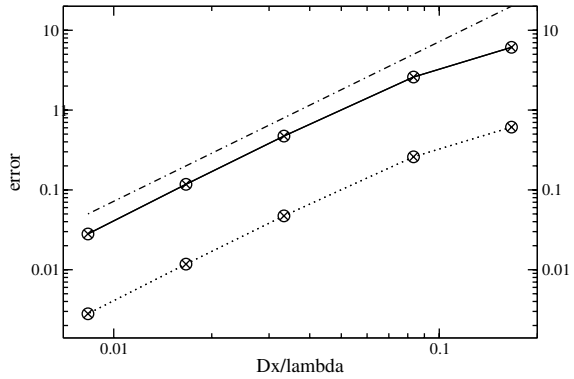

Fig. 1. Linear acoustics. Spatial error for the pressure (multiplied by 10, solid line) and for the velocity (dotted line), without inner loop (circles) or with two iterations in the inner loop (crosses). The error is given as a function of the cell spacing divided by the wave width. The dashed-dotted line represents the second-order slope.

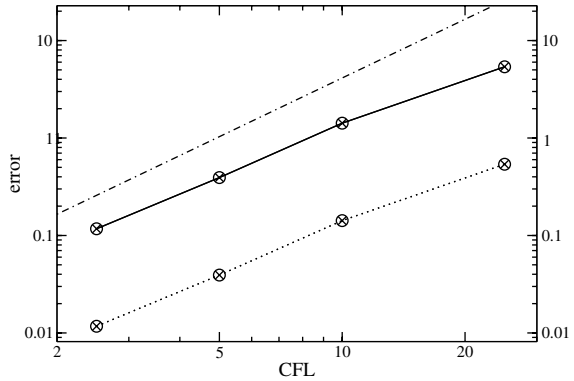

Fig. 2. Linear acoustics. Temporal error for the pressure (multiplied by 10, solid line) and for the velocity (dotted line), without inner loop (circles) or with two iterations in the inner loop (crosses). The dashed-dotted line represents the second-order slope.

4.1.2. Low-Mach advection

A vortex with a low-Mach number ($Ma = 0.1$) is propagated on a periodic mesh. Then, the L2 error is measured after one convective time. Fig. 3 presents the spatial error as a function of the mesh resolution. As expected, the second-order convergence is obtained without any inner-loop.

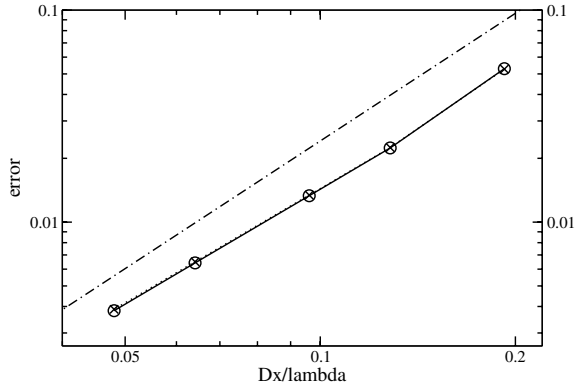

Fig. 3. Low-Mach advection. Spatial error for the velocity without inner loop (solid line and circles) or with two iterations in the inner loop (dotted line and crosses). The error is given as a function of the cell spacing divided by the vortex width. The dashed-dotted line represents the second-order slope.

4.2. Unresolved homogeneous isotropic turbulence

Computations of unresolved homogeneous isotropic turbulence at infinite Reynolds number were used by [16] to evaluate the numerical non-linear stability of different explicit methods. In the limit $Re \to \infty$, the Navier–Stokes equations tend to the Euler equations, and the kinetic energy should be conserved. With the proposed method and the incompressible solver described in Section 2.1, different homogeneous isotropic turbulence (HIT) computations are performed on a 32^3 Cartesian grid by solving the Euler equations and by starting from the same initially turbulent field. The turbulent Mach number of the initial field is *0.07* and the initial non-dimensionalized wave number is $k_0 = 6$. Most of the initial vortices are resolved with only five points. The time-step is kept constant during the computations. The kinetic-energy decay for three different initial acoustic CFL numbers is given in Fig. 4. For this extreme case, the computations do not blow up, but the kinetic-energy is dissipated instead of remaining constant. Nevertheless, for the highest CFL, 80% of the energy is kept after the first eddy turn-over time. It must also be noted that most of the dissipation occurs after the first eddy turn-over time when the vortices are very poorly resolved on the mesh. When the vortices are better resolved, i.e. with more than four points, the dissipation is very small. Since a strictly kinetic-energy conserving scheme is used in the predictor steps, the kinetic-energy decay is caused by the fourth-order dissipation of the pressure gradient term in the correction steps [14]. This fourth-order dissipation is due to the interpolation of the pressure in the gradient operator, which is needed for collocated schemes. Since the same numerical operator is used in the two different solvers, the kinetic-energy decay is

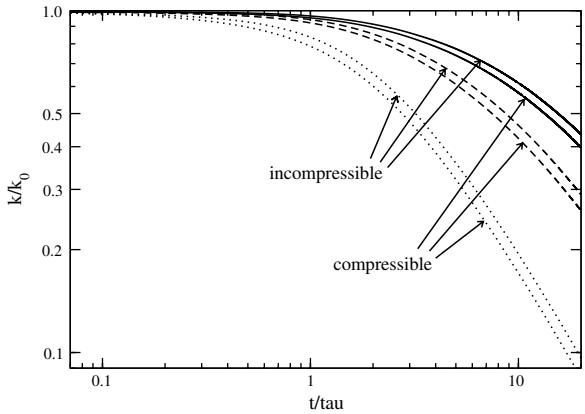

Fig. 4. Unresolved HIT. Kinetic-energy decay versus time (non-dimensionalized by the eddy turn-over time) for different acoustic CFL numbers. (——) $CFL_0 = 0.5$, (---) $CFL_0 = 1$, (· · · · · ·) $CFL_0 = 5$.

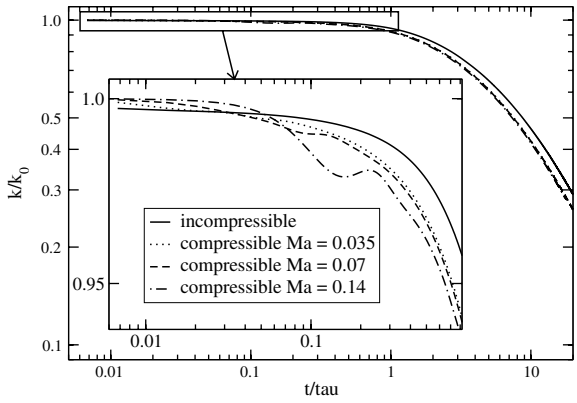

Fig. 5. Unresolved HIT. Kinetic-energy decay versus time (non-dimensionalized by the eddy turn-over time) for different *Ma* numbers.

similar in the two cases for a same acoustic CFL number. The small difference between the incompressible and compressible solvers is investigated in Fig. 5. This figure presents three compressible computations at different Mach numbers for an acoustic CFL number set equal to unity. It shows that the kinetic-energy decay is independent on the Mach number except during the very first time-steps. In these early time-steps, acoustic waves are generated because of the initialization of the compressible computations with a constant pressure field not adapted with the turbulent velocity field. These acoustic waves do not exist in the incompressible computation because the pressure field is entirely determined from the predicted velocity. The kinetic-energy decay difference between the two solvers may be explained by the kinetic energy needed to generate these acoustic waves.

4.3. Cold flow of a lean-premixed swirl-burner

4.3.1. Description

The presented method is applied in the LES computation of the cold flow of an industrial burner [17]. The objectives of this test case are to demonstrate that the present solver is able to compute efficiently a low-Mach number flow with an accuracy similar to the equivalent incompressible solver while predicting a low-order acoustic mode of the cavity.

The industrial burner features a plenum, a swirler, and a combustion chamber. A three-million hexahedral-based mesh is used. The dynamic Smagorinsky model [18,19] is used in the sub-filter closure models. Fig. 6

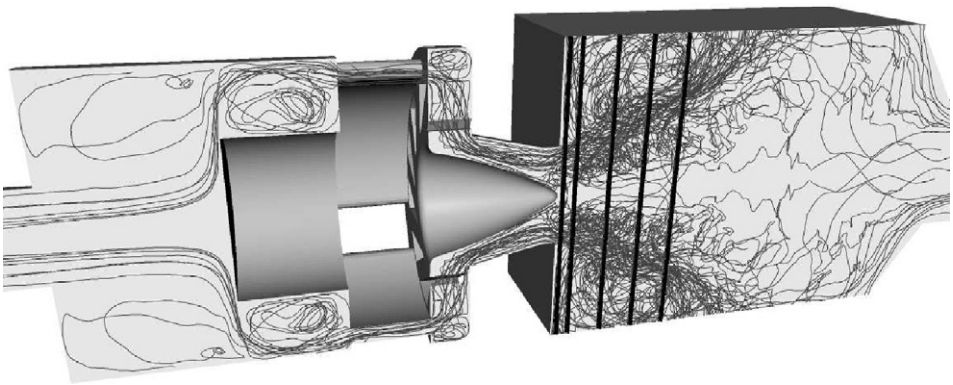

Fig. 6. Swirl-burner. Azimuthally-projected stream-lines and velocity-data measurement locations.

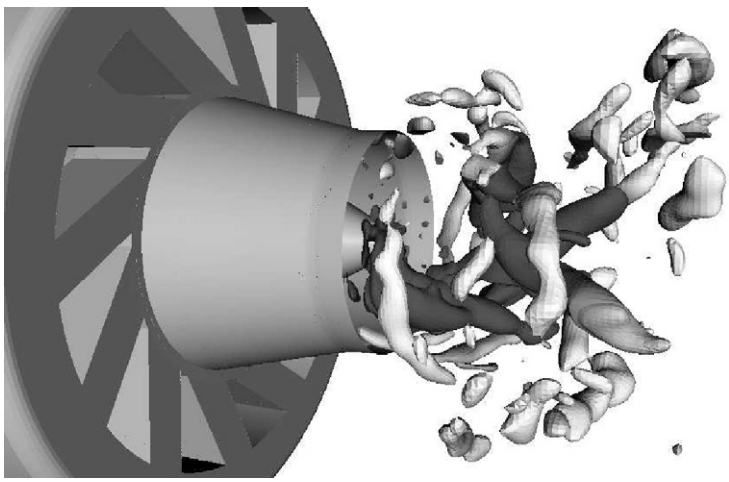

Fig. 7. Swirl-burner. Coherent structures colored by the axis distance. The main hydrodynamic instability consists of the dark structures anchored on the injector head.

shows instantaneous streamlines of the flow obtained with the new compressible solver. The main recirculation zones and the spreading rate of the swirling flow are clearly represented. The acoustic CFL number of the computation is set to a fixed value, $CFL = 7$. A computation with the same mean convective CFL, $CFL_{conv} = 0.41$, is also performed with an incompressible solver that uses the same temporal and spatial schemes. The compressible solver is only 25% more CPU expensive than the incompressible solver. This is a consequence of the fact that no inner loop is needed to correctly represent the main features of the flow. This over-cost is mainly due to the density and to the enthalpy, which are not transported in the incompressible solver. But this over-cost is slightly balanced by the fact that the Helmholtz equation is efficiently inversed by the BiCGStab solver whereas the Poisson equation is more difficult to inverse on unstructured grids with the algebraic multi-grid solver.

4.3.2. Dynamic behavior

Roux et al. [17] have shown that the cold flow of the burner features a hydrodynamic instability. The instability they have analyzed has the structure of a Precessing Vortex Core (PVC). In the present computation, a strong hydrodynamic instability is also found, but as shown in Fig. 7, its structure is more complex than a single PVC. It consists of two to three interlaced vortices. The differences between the instability structures likely arise from the fact that the hexahedral-based mesh used in this study is finer in the injector head region than the tetrahedral-based mesh. In the LES computation, the frequency of the hydrodynamic mode is obtained by placing a pressure probe close to the injector head. The Fourier transform of the pressure signal

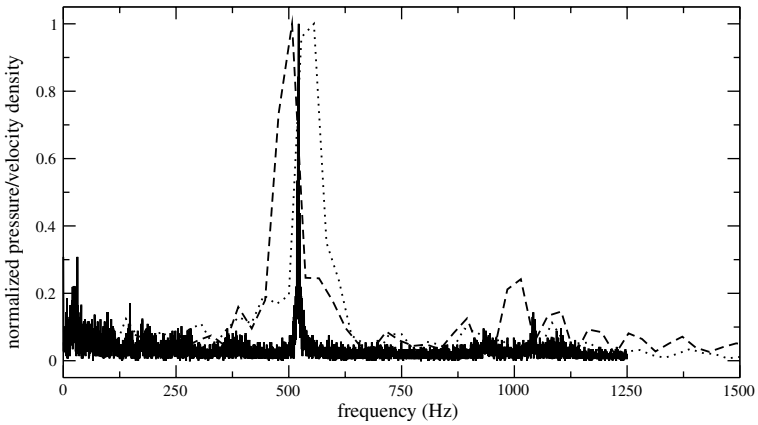

Fig. 8. Swirl-burner. Hydrodynamic-mode frequency. (——) experiments, (- - -) compressible LES, (· · · · · ·) incompressible LES.

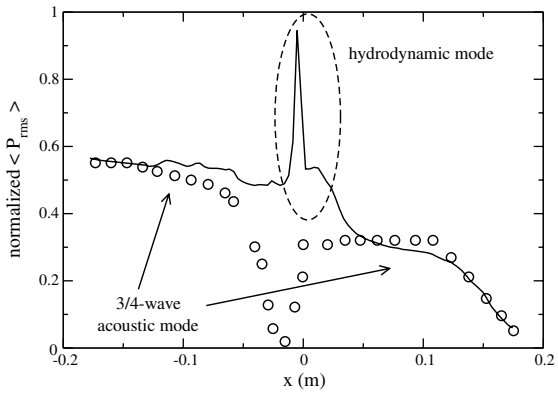

Fig. 9. Swirl-burner. Normalized mean pressure fluctuations along the main axis. (○) Helmholtz computation from [17], (——) compressible LES.

is compared to the experimental data in Fig. 8 for the incompressible and compressible solvers. The computations predict a frequency close to the experimental value of 520 Hz.

To highlight the main benefit of the compressible solver over the incompressible solver, the pressure fluctuations are averaged and normalized on constant-abscissa planes along the main axis and plotted in Fig. 9. In this figure, the pressure fluctuations predicted by the Helmholtz solver used in Roux et al. [17] for the 3/4-wave longitudinal mode are also presented. This mode is the only low-order unstable mode for the isothermal case and the complete analysis of all the cavity modes present in this industrial burner can be found in Roux et al. [17]. The two main modes of the burner are clearly represented by the compressible solver. The pressure fluctuations peak around $x = 0$, which corresponds to the head of the combustion chamber. This peak is due to the hydrodynamic instabilities issued from the injector head. The remaining contribution comes from one of the low-order longitudinal acoustic mode of the device. This 3/4-wave mode, which strongly depends on the

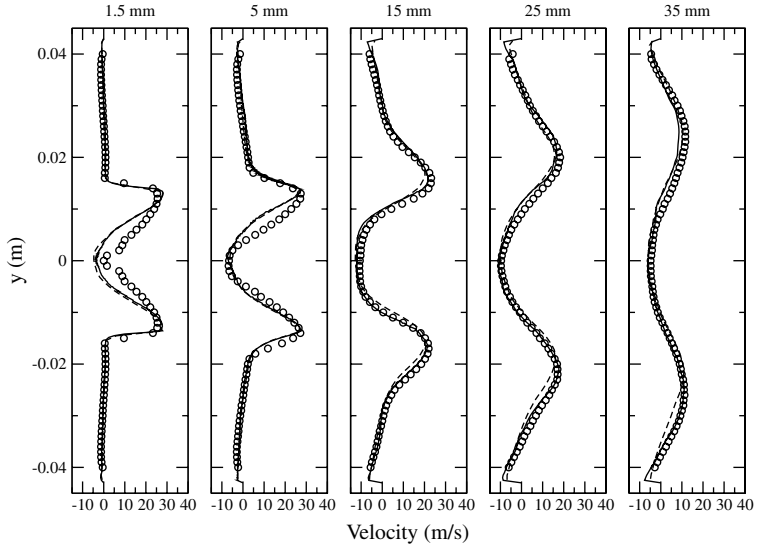

Fig. 10. Swirl-burner. Mean axial velocity profiles. (○) experiments, (——) compressible LES, (---) incompressible LES.

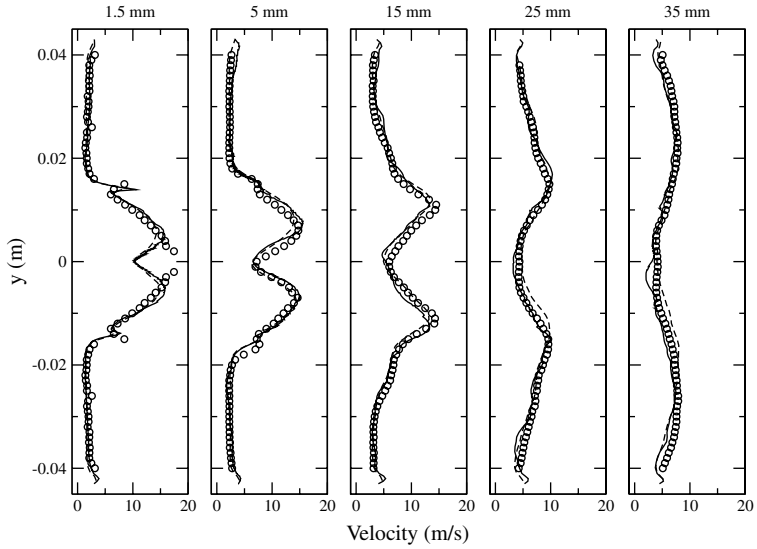

Fig. 11. Swirl-burner. Axial velocity RMS profiles. (○) experiments, (——) compressible LES, (---) incompressible LES.

speed of sound and on the acoustic reflections, can only be captured by a compressible solver. It may be noted that the pressure fluctuations given by the incompressible solver can not be processed in the same manner because in the case of incompressible flows only the pressure gradient is meaningful. The Poisson equation has indeed an infinite number of solutions that all differ by a constant.

4.3.3. Velocity statistics

Velocity statistics of LDV measurements and of the LES computations are compared in Figs. 10–15. The five comparison locations are given in Fig. 6. The mean and RMS velocities are in very good agreement for the five locations, except in a zone close to the head of the injector. This phenomenon arises from the fact that there is an uncertainty about the azimuthal position of the LDV measurements. It explains why the statistics far from the injector are in agreement while there are some differences close to the injector. It can also be noted that the LES computations cannot capture the steep gradient of the mean azimuthal velocity far from the

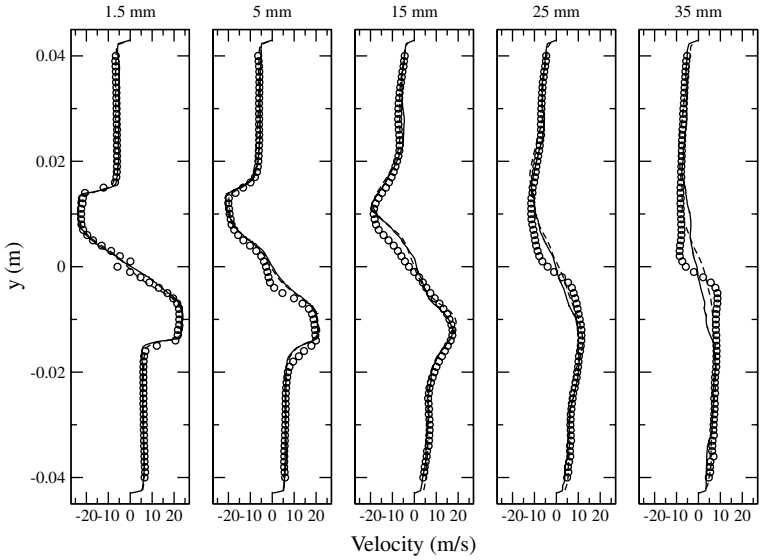

Fig. 12. Swirl-burner. Mean azimuthal velocity profiles. (○) experiments, (——) compressible LES, (---) incompressible LES.

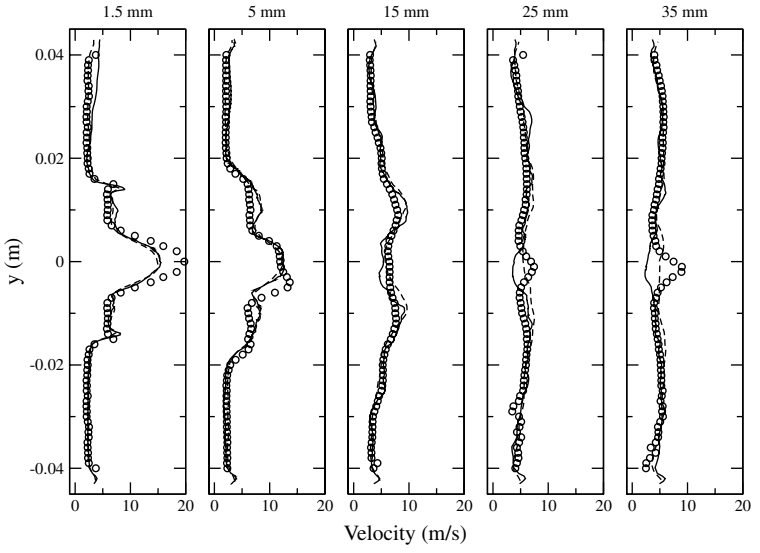

Fig. 13. Swirl-burner. Azimuthal velocity RMS profiles. (○) experiments, (——) compressible LES, (---) incompressible LES.

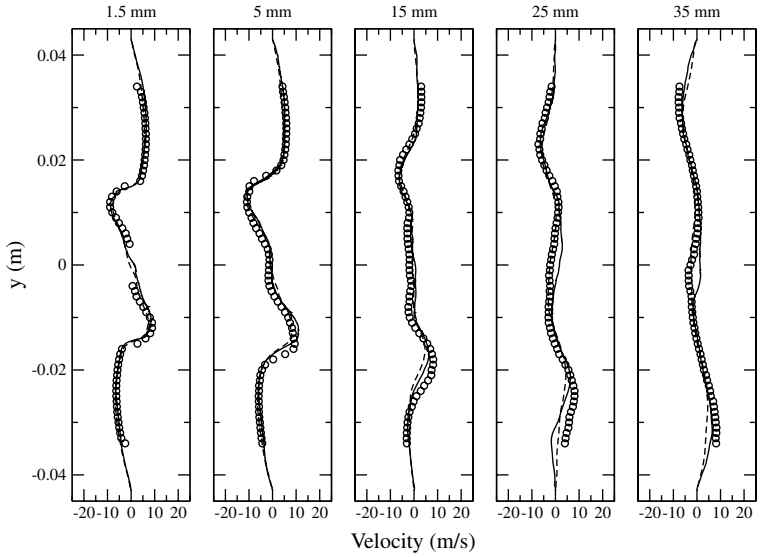

Fig. 14. Swirl-burner. Mean radial velocity profiles. (○) experiments, (——) compressible LES, (---) incompressible LES.

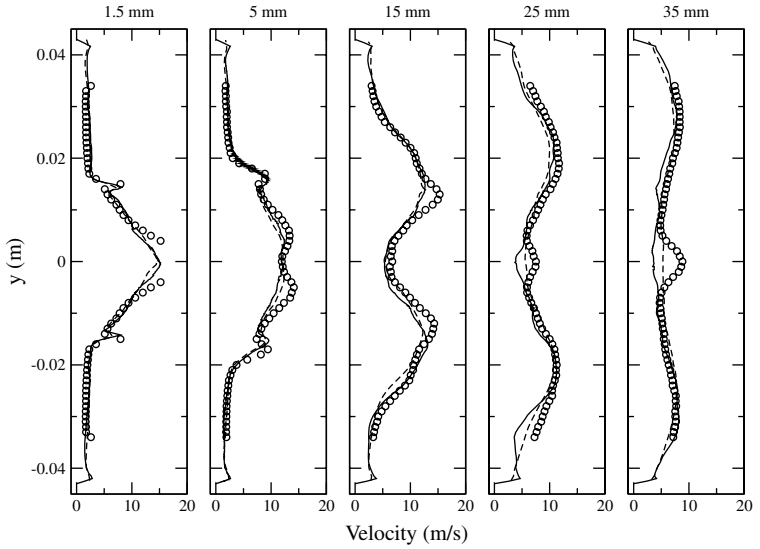

Fig. 15. Swirl-burner. Radial velocity RMS profiles. (○) experiments, (——) compressible LES, (---) incompressible LES.

injector. A better resolution may be needed in this region to predict this gradient. Finally, the incompressible and compressible computations give similar results meaning that the 3/4-wave acoustic mode, which is not captured by the incompressible solver, has no influence on the velocity statistics. This wouldn't be the case for an unstable reacting burner. The small differences may be due to the fact that the physical duration of the incompressible computation is 12 flow-through times whereas the physical duration of the compressible computation is eight flow-through times, a flow-through time being equal to 0.01 s. The statistics of the compressible computation are therefore slightly less converged than the incompressible ones.

5. Conclusions

A new semi-implicit compressible solver for LES in complex geometries has been developed. The fractional-step method used in the solver is obtained from a characteristic splitting of the Navier–Stokes equations. This

physical splitting allows for the numerical separation of the acoustics from advection. The acoustics are therefore treated implicitly to remove the acoustic CFL limit. The proposed method is very efficient because it does not require inner iterations to achieve a second-order accuracy for both linear acoustics and low-Mach advection. In the low-Mach limit, the solver tends towards an incompressible solver, inheriting the same stability and efficiency properties. A kinetic-energy conserving scheme is used for the discretization of the convective terms, leading to a kinetic-energy conserving solver in the low-Mach limit. These properties have been illustrated and confirmed on simple test cases. The new solver has been applied in the LES computation of the cold flow of an industrial burner. The velocity statistics from the LES computation are in very good agreement with experimental data. The dynamic behavior of the flow has also been discussed. The performance of the compressible solver has been compared to an incompressible solver featuring the same discretization schemes. The compressible solver has been found to be only 25% more CPU expensive than the incompressible solver, while more physics are represented. Therefore, the new solver fulfills the essential requirements for efficiency, accuracy and stability.

Acknowledgments

The authors gratefully acknowledge funding by SAFRAN Group and the US Department of Energy within the ASCI program.

References

[1] E. Turkel, R. Radespiel, N. Kroll, Assessment of preconditioning methods for multidimensional aerodynamics, Comput. Fluids 26 (6) (1997) 613–634.
[2] H. Guillard, C. Viozat, On the behaviour of upwind schemes in the low Mach number limit, Comput. Fluids 28 (1) (1998) 63–86.
[3] E. Turkel, Preconditioned methods for solving the incompressible low speed compressible equations, J. Comput. Phys. 72 (2) (1987) 277–298.
[4] Y.H. Choi, C.L. Merkle, The application of preconditioning in viscous flows, J. Comput. Phys. 105 (2) (1993) 207–223.
[5] F.H. Harlow, A.A. Amsden, Numerical calculation of almost incompressible flow, J. Comput. Phys. 3 (1) (1968) 80–93.
[6] K.C. Karki, S.V. Patankar, Pressure based calculation procedure for viscous flows at all speeds in arbitrary configurations, AIAA J. 27 (9) (1989) 1167–1174.
[7] S.Y. Yoon, T. Yabe, The unified simulation for incompressible and compressible flow by the predictor–corrector scheme based on the CIP method, Comput. Phys. Commun. 119 (1999) 149–158.
[8] O.C. Zienkiewicz, P. Nithiarasu, R. Codina, M. Vazquez, P. Ortiz, Characteristic-based-split procedure: an efficient and accurate algorithm for fluid problems, Int. J. Numer. Methods Fluids 31 (1) (1999) 359–392.
[9] C. Wall, C.D. Pierce, P. Moin, A semi-implicit method for resolution of acoustic waves in low Mach number flows, J. Comput. Phys. 181 (2) (2002) 545–563.
[10] J. Kim, P. Moin, Application of a fractional-step method to incompressible Navier–Stokes equations, J. Comput. Phys. 59 (2) (1985) 308–323.
[11] K. Mahesh, G. Constantinescu, P. Moin, A numerical method for large-eddy simulation in complex geometries, J. Comput. Phys. 197 (1) (2004) 215–240.
[12] C. Pierce, P. Moin, Progress-variable approach for large-eddy simulation of turbulent combustion, Ph.D. thesis, Mech. Eng. Dept. Rep. TF-80. Stanford University, 2001.
[13] C. Pierce, P. Moin, Progress-variable approach for large eddy simulation of non-premixed turbulent combustion, J. Fluid Mech. 504 (2004) 73–97.
[14] F. Ham, G. Iaccarino, Energy conservation in collocated discretization schemes on unstructured meshes, in: Annual Research Briefs, Center for Turbulence Research, NASA Ames/Stanford University, 2004, pp. 3–14.
[15] T. Poinsot, S. Lele, Boundary conditions for direct simulations of compressible viscous flows, J. Comput. Phys. 101 (1) (1992) 104–129.
[16] A.E. Honein, P. Moin, Higher entropy conservation and numerical stability of compressible turbulence simulations, J. Comput. Phys. 201 (2) (2004) 531–545.
[17] S. Roux, G. Lartigue, T. Poinsot, U. Meier, C. Berat, Studies of mean and unsteady flow in a swirled combustor using experiments, acoustic analysis, and large eddy simulations, Combust. Flame 141 (1–2) (2005) 40–54.
[18] M. Germano, U. Piomelli, P. Moin, W.H. Cabot, A dynamic subgrid-scale eddy viscosity model, Phys. Fluids 3 (7) (1991) 1760–1765.
[19] D.K. Lilly, A proposed modification on the Germano subgrid-scale closure method, Phys. Fluids 4 (3) (1992) 633–635.